High-mobility transparent conductive thin films of cerium-doped hydrogenated indium oxide

3 authors, including:

Eiji Kobayashi
Kishu Giken Kogyo CO. Ltd.
15 PUBLICATIONS   **387** CITATIONS

SEE PROFILE

Yoshimi Watabe
Choshu Industry
23 PUBLICATIONS   **374** CITATIONS

SEE PROFILE

Some of the authors of this publication are also working on these related projects:

Silicon heterojunction solar cell View project

Transparent conducive oxide View project

High-mobility transparent conductive thin films of cerium doped hydrogenated indium oxide

Eiji Kobayashi[1], Yoshimi Watabe[1], and Tetsuya Yamamoto[2]

[1]Choshu Industry Co., Ltd., 3740, Shin-yamanoi, Sanyo Onoda, Yamaguchi 757-8511, Japan

[2]Kochi University of Technology, 185 Miyanokuchi, Tosayamada-cho, Kami, Kochi 782-8502, Japan

E-mail: e.kobayashi@choshu.co.jp

We have developed 100-nm-thick cerium-doped hydrogenated indium oxide (ICO:H) films with superior Hall mobility of 130-145 $cm^2V^{-1}s^{-1}$. The ICO:H films deposited at 150 deg C by ion-plating with dc arc discharge were post annealed at 200 deg C. The relationship between Hall mobility and carrier density of the polycrystalline ICO:H films shows that carrier transport were limited by ionized impurity scattering mechanism in the intra-grains. The surfaces of the ICO:H films were found to be very smooth and clear grain-boundary area were not observed.

High carrier mobility of transparent conductive oxide (TCO) films for solar cells is required to be coexistent with high optical transparency and low ohmic loss in consequence of light absorption loss in the near-infrared (NIR) region caused by plasma oscillation in proportion to free-carrier density[1]. Koida *et al.* showed that highly hydrogen-doped In_2O_3 (IO:H) exhibited Hall mobility exceeding 100 cm$^2 \cdot$V$^{-1} \cdot$s^{-1}.[2] Various dopants of metal species such as W[3], Zr[4], and Mo[5] have been used to dope polycrystalline In_2O_3 films to improve crystallinity with reduction of lattice defects in intra-grains. We have been investigating the properties of Ce[6] doped In_2O_3 films. The research is based on two factors with the effects: (i) effective ionic radius of Ce^{4+} with coordination number of 6 (0.101 nm)[7] is closed to that of In^{3+} with coordination number of 6 (0.094 nm)[7], leading to the reduction of microstrain in the vicinity of the dopant sites; (ii) the density of oxygen vacancy can be reduced by doped CeO_2 with large standard enthalpy of formation compared with In_2O_3, causing the improvements of the crystallinity. In this letter, we clarify effects of hydrogen-doping with Ce incorporated and post annealing on structural and electrical properties of ICO:H films.

100-nm-thick In_2O_3-based TCO films were deposited by ion-plating (IP) with dc-arc discharge [8]. In_2O_3 with CeO_2 (ICO) contents of 3 wt.% and pure In_2O_3 (IO) pellets (Sumitomo Metal Mining Co., Ltd.) were used as resource materials. The films were deposited on Corning Eagle XG glass substrates at 150 °C. The deposition gases were Ar, O_2 (8-13 vol.%), and H_2 (0-2 vol.%) and the total gas pressure during film deposition was 0.45 Pa. Ultimate vacuum pressure of the process chamber before the deposition was 1 x 10^{-4} Pa or below. The compositions of the films were analyzed with Rutherford Backscattering Spectrometry (RBS) and Hydrogen Forward Scattering (HFS) using a CEA manufactured RBS system. The structural properties were analyzed by grazing incidence XRD scans using MRS 6-axis diffractometer (PANalytical X'Pert Pro) equipped with a Cu X-ray tube and parallel-beam optics. Electric conductivity and Hall voltage were measured with a Hall effects measurement system (Toyo Technica, ResiTest 8300). Grain size of the films was observed with a field-emission scanning electron microscope (FE-SEM, Hitachi High-Tech, SU8240). The surface morphology was characterized by an atomic force microscopy (Park Systems, NX20).

Table I summarizes In, Ce, O, and H compositions determined by RBS and HFS measurements for the 100-nm-thick ICO and ICO:H films deposited with H_2/gas flow ratio of 0 % and 1.0 % and identical oxygen partial pressure, respectively. Those films were post-annealed at 200 °C for 30 minutes in air. Note that little difference in Ce compositions between the two films deposited by different processes was observed. In addition, Table I shows that both ICO and ICO:H films show oxygen-rich in contrast with stoichiometric composition of In_2O_3. As mentioned below, analysis of data obtained by XRD measurements of the two films above shows no segregation of Ce-oxides such as CeO_2 and Ce_2O_3 in those films. We confirmed the effect of Ce doping on the control of O composition in the films described above; the density of oxygen vacancy in the intra-grains can be reduced. Taking into account of the fact that oxygen interstitial with electron affinity would act as *n*-type killer in the intra-grains and chemisorbed

oxygen species with a negative charge, O^-, at the grain boundaries would form a barrier height to cause free-carrier scattering, resulting in the reduction of carrier mobility, the O composition in the films must be controlled. Table I proves that codoping of H with Ce donors with increasing H_2/gas flow ratio leads to an increase in H compositions together with a slight decrease in the atomic ratio of O species. This indicates that O composition in ICO matrix can be controlled systematically by changing the H_2/gas flow ratio with a Ce doping content during the deposition combined with the post annealing. The technique with the codoping mixed with the post annealing can work very well because it can enhance carrier transport due to the improvements of the microstructure in the intra-grains and reduction of the contribution of grain-boundary scattering mechanism to the carrier transport. This will be discussed below.

Fig.1 shows grazing incidence XRD patterns of the ICO and ICO:H films with different H_2/gas flow ratios. All the films were post-annealed at 200 °C for 30 minutes in air. The incidence angle was fixed at 1.0 degree. These data were plotted with a logarithmic intensity scale to overemphasize many weak peaks in the patterns. No peaks of Ce-oxides such as CeO_2 and Ce_2O_3 were observed. We investigated the effects of the post annealing and H doping on the crystal structure, microstructure such as lattice parameters and residual strain.

Note that no peaks of as-deposited ICO:H films were observed. We found the effect of the post annealing on the structure of the films. The amorphous phase of as-deposited ICO:H films changed to bixbyte In_2O_3 polycrystalline: the angles of diffracted peaks were almost identical to those of ITO containing 6.25% Sn (dotted line)[9].

Firstly, lattice parameters (ls) were estimated from all peaks that were identified with each film. Then, the lattice parameter (L) was defined as an average value of the ls. In addition, the residual strain (S) in each film was calculated on the basis of the size-strain analysis of the peak data obtained by the strain model. The L and S values in each film are shown in Fig. 1. We found the effects of H doping on the reduction of both L and S values of the ICO films.

Fig.2 shows the relationship between Hall mobility (μ_H) and carrier density (N) for the post-annealed ICO and ICO:H films with H_2/gas flow ratios in the range of 1.0% to 2.0%. For comparison, the data for the post-annealed IO:H with H_2/gas flow ratios in the range of 1.0% to 2.0% were added. Note that the Hall motility of the ICO:H films with a H_2/gas flow ratio of 1.0% shows higher values of 130-145 $cm^2V^{-1}s^{-1}$ than those of the IO:H films.

The carrier mobility limited by ionized impurity scattering, μ_I, was calculated by the Brooks-Herring-Dingle (B-H-D) theory[10, 11] with both degeneracy and non-parabolicity of the conduction bands[12]. On the other hand, the carrier mobility limited by grain boundary scattering, μ_G, was calculated based on Seto theory[14]. With increasing N up to $\sim 1 \times 10^{20}$ cm^{-3}, μ_I is larger than μ_G. With further increasing N, μ_G is larger than μ_I. Note that the expression of $\mu_H^{-1} = \mu_G^{-1} + \mu_I^{-1}$ cannot explain μ_H of ICO:H

films with H_2/gas flow ratio of 1.0%. The experimental data and the expression above implies that μ_G value is very large compared with μ_I one. We thus concluded that ionized impurity scattering mechanism is a dominant factor limiting the carrier mobility in such films. Fig. 2 shows that the expression above explains μ_H behavior of the other ICO:H films, ICO:H films with H_2/gas flow ratios of 1.5% and of 2.0%, and ICO films very well. It can be concluded that both ionized impurity scattering and grain boundary scattering mechanism determine the carrier mobility of those films. In addition, it should be mentioned that the two ICO:H films with H_2/gas flow ratios of 1.5% and of 2.0% have both the crystals-grown area and the amorphous area, as discussed below. In such films with the mixed structures, the scattering mechanism in the amorphous area also contributes to the carrier transport in the films. On the other hand, for IO:H films, more study must be required.

Fig. 3 shows the back scattered electron (BSE) images of the surface structures of ICO, ICO:H, and IO:H films captured by FE-SEM. The grains of the post-annealed ICO film were clearly observed with 100 nm or below in size, as shown in Fig. 3(a). The grain boundaries of the as-deposited ICO:H film with a H_2/gas flow ratio of 1.0% were not clearly observed (Fig. 3(b)). Note that Figs. 3 (c) and (d) show conspicuous grains with kaleidoscope patterns for the post-annealed ICO:H films. Figs. 3(e) and (f) show both the crystals-grown area and the amorphous area for the post-annealed ICO:H with a H_2/gas flow ratio of 1.5%. This was consistent with Fig. 1(c). The grains of the post-annealed IO:H film deposited with a H_2/gas flow ratio of 1.0% were observed to be over 1 μm in size (Fig. 3(g)), whereas the grains in the post-annealed IO:H film with H_2/gas flow ratio of 2.0% were not clear as well as the ones in ICO:H films deposited with H_2/gas flow ratio of 1.0% mentioned above.

Fig. 4 shows the AFM images of post-annealed ICO, as-deposited and post-annealed ICO:H with H_2/gas flow ratio of 1.0%. The one-dimensional cross section scans of surface profiles are added in Fig. 4. We assumed that the signals with 2 nm height or higher within the field were particles generated from glass substrates when they were scrubbed. The results of AFM with the calculated average surface roughness (R_a) and root-mean-square roughness (R_q) show that the surface of the post-annealed ICO:H film was smoother than those of other films. Spiky signals with height of 1 to 2 nm were observed on the surface of the film. Note that the R_a value excluding the signals was just 0.232 nm (see Fig. 4(f)). The spiky signals cannot be identified from the analysis of data obtained by FE-SEM and AFM measurements; whether it originates in the particles or projections from the film. On the other hand, island structures with 1-nm height were observed on the surface of the as-deposited ICO:H film (see Fig. 4(b)). The R_a values of internal and external island structures were 0.257 nm and 0.266 nm, respectively (see Fig. 4(e)). Taking into the account of the fact that annealed films had smoother surfaces than as-deposited films, as shown Figs. 4(b) and (c), we concluded that those island structures on the as-deposited ICO film disappeared thorough annealing: the atoms in the island structures moved inside

the film during the recrystallization from the solid phase during the annealing process. The post annealing technique in this work is a key to achieve ICO:H films having high Hall mobility together with smooth surface.

We have obtained the following result in this experiment. 100-nm-thick post-annealed ICO:H films deposited by ion plating at 150 °C show superior Hall mobility of 130-145 $cm^2 \cdot V^{-1} \cdot s^{-1}$. The films exhibit very smooth surface. Analysis of the relationship between Hall mobility and carrier density shows that the dominant factor limiting the carrier transport of the films is ionized impurity scattering mechanism in the intra-grains. The findings prove that the films have great potential for application in solar cells.

This is the post-print version of the following article: Applied Physics Express, Volume 8, Number 1 , which has been published in final form at
http://iopscience.iop.org/article/10.7567/APEX.8.015505

[1] I. Hamberg and C. G. Granqvist, J. Appl. Phys. **60** (1986) R123.

[2] T Koida, H Fujiwara, M Kondo, J. Non-Cryst. Solids **354** (2008) 2805.

[3] P. F. Newhouse, C.-H. Park, and D. A. Keszler, J. Tatea, P. S. Nyholm, Appl. Phys. Lett. **87** (2005) 112108.

[4] T. Koida, M. Kondo, J. Appl. Phys. **101** (2007) 063705.

[5] Y. Meng, X. Yang, H. Chen, J. Shen, Y. Jiang, Z. Zhang, Z. Hua, Thin Solid Films **394** (2001) 219.

[6] N. Mori, J. Ueno, Y. Uesugi, and K. Miki, e-J. Surf. Sci. Nanotech. **10** (2012) 471.

[7] R. D. Shannon, Acta Cryst. **A32** (1976) 781.

[8] Y. shigesato. S. Takaki and T. Haranoh, J. Appl. Phys. **71** (1992) 3356.

[9] N. Nadaud, N. Lequeux, M. Nanot, J. Jove and T. Roisnel, J. Solid State Chem. **135** (1998) 140.

[10] H. Brooks, Phys. Rev. **79** (1950) 1013.

[11] R. B. Dingle, Phil. Mag. **46** (1955) 831.

[12] T. Pisarkiewicz, K. Zakrzewska, and E Leja, Thin Solid Films **174** (1989) 217.

[13] J. Y. W. Seto, J. Appl. Phys. **46** (1975) 5247.

Table I. In, Ce, O, and H compositions of ICO and ICO:H films with post annealing at 200 °C.

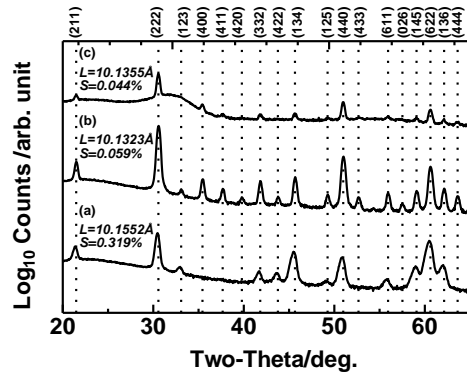| H$_2$/gas flow ratio (%)	In	Ce	O	H
		(at.%)		
0	34.0	0.7	64.6	0.7
1.0	35.7	0.6	62.4	1.3

Fig. 1. Grazing incidence XRD profiles for (a) ICO, (b) ICO:H with a H_2/gas flow ratio of 1.0%, (c) ICO:H with a H_2/gas flow ratio of 1.5%. All the films were post annealed at 200 °C for 30 minutes in air.
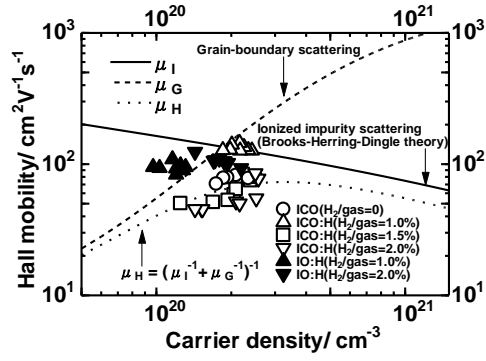
Fig. 2. Hall mobility versus carrier density of ICO, ICO:H, and IO:H films with post annealing at 200 °C for 30 minutes in air.
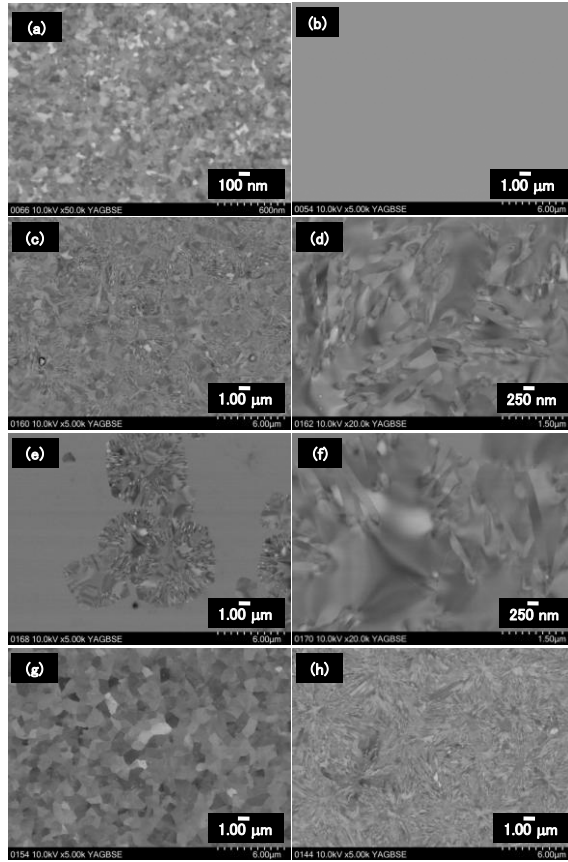
Fig. 3. Back scattered electron (BSE) images of the surface morphologies of (a) post-annealed ICO, (b) as-deposited ICO:H with H_2/gas flow ratio of 1.0%, (c)-(d) post-annealed ICO:H with H_2/gas flow ratio of 1.0%, (e)-(f) post-annealed ICO:H with H_2/gas flow ratio of 1.5%, (g) post-annealed IO:H with H_2/gas flow ratio of 1.0%, and (h) post-annealed IO:H with H_2/gas flow ratio of 2.0%. The post-annealing was performed at 200 °C for 30 minutes in air.
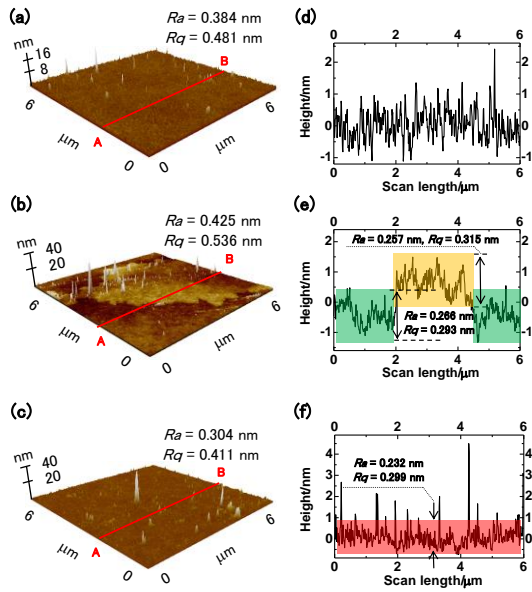
Fig. 4. AFM images of (a) post-annealed ICO, (b) as-deposited ICO:H with a H_2/gas flow ratio of 1.0%, (c) post-annealed ICO:H with a H_2/gas flow ratio of 1.0%, and (d)-(f) line scan profiles (A-B lines) corresponding to (a)-(c), respectively. The post-annealing was performed at 200 °C for 30 minutes in air. The average surface roughness (R_a) and root-mean-square roughness (R_q) are also shown.

11